minerals

MDPI

Article

Fluid Inclusions and C–H–O–S–Pb Isotopes of the Huoluotai Porphyry Cu (Mo) Deposit in the Northern Great Xing'an Range, NE China: Implications for Ore Genesis

Yonggang Sun [1,2], Bile Li [2,*], Xusheng Chen [3], Fanbo Meng [3], Qingfeng Ding [2], Ye Qian [2,4] and Linlin Wang [2,4]

[1] School of Resources and Civil Engineering, Suzhou University, Suzhou 234000, China
[2] College of Earth Sciences, Jilin University, Changchun 130061, China
[3] Qiqihaer Institute of Geological Exploration, Heilongjiang 161006, China
[4] Key Laboratory of Mineral Resources Evaluation in Northeast Asia, Ministry of Land and Resources, Changchun 130061, China
* Correspondence: libl@jlu.edu.cn

Abstract: The Huoluotai Cu (Mo) deposit is a recently discovered porphyry Cu deposit in the northern Great Xing'an Range, NE China. Fluid inclusion (FI) micro-thermometry results and the C–H–O–S–Pb isotope compositions of the Huoluotai Cu (Mo) deposit are presented in this study. The ore-forming process consists of the sulfide-barren quartz stage (I), the quartz + chalcopyrite ± pyrite ± molybdenite stage (II), the quartz + polymetallic sulfide stage (III), and the quartz + calcite ± pyrite ± fluorite stage (IV). Cu mineralization occurred mainly in stage II. Four types of FIs were recognized: liquid-rich two-phase FIs (L-type), vapor-rich two-phase FIs (V-type), daughter-mineral-bearing three-phase FIs (S-type), and CO_2-bearing FIs (C-type). In stage I, the ore-forming fluids belong to an $H_2O-NaCl-CO_2$ system. In stages II, III, and IV, the ore-forming fluids belong to an $H_2O-NaCl$ system. The results of the FI micro-thermometry and H–O isotope analysis show that the ore-forming fluids originated from a magmatic origin in stage I and mixed with meteoric water from stages II to IV. The S–Pb isotope results suggest that the source of the ore-forming materials has the characteristics of a crust–mantle-mixing origin. Fluid boiling occurred in stages I and II. The FI micro-thermometric data further show that Cu was mainly deposited below 400 °C in stage II, suggesting that fluid boiling occurring below 400 °C may be the primary factor for Cu precipitation in the Huoluotai Cu (Mo) deposit.

Keywords: northern Great Xing'an Range; Huoluotai Cu (Mo) deposit; fluid inclusions; C–H–O–S–Pb isotope; fluid boiling

Citation: Sun, Y.; Li, B.; Chen, X.; Meng, F.; Ding, Q.; Qian, Y.; Wang, L. Fluid Inclusions and C–H–O–S–Pb Isotopes of the Huoluotai Porphyry Cu (Mo) Deposit in the Northern Great Xing'an Range, NE China: Implications for Ore Genesis. *Minerals* **2022**, *12*, 1072. https://doi.org/10.3390/min12091072

Academic Editor: Jan Marten Huizenga

Received: 20 July 2022
Accepted: 24 August 2022
Published: 25 August 2022

1. Introduction

As one of the largest orogenic collages in the world, the Central Asian Orogenic Belt (CAOB) is located between the East Europe, Siberia, Tarim, and North China cratons (Figure 1A). The northern Great Xing'an Range (NGXR) is tectonically located in the eastern segment of the CAOB (Figure 1A,B) and hosts a number of epithermal and orogenic Au, hydrothermal Ag–Pb–Zn, porphyry, and skarn Pb–Zn deposits (Figure 1C). Over the past decade, many late Mesozoic porphyry deposits in the NGXR have been discovered and raised concern (Figure 1C). Examples include the Daheishan Mo (ca. 147 Ma; [1]), the Chalukou Mo (ca. 148 Ma; [2]), the Fukeshan Cu (Mo) (ca. 149 Ma; [3,4]), and the Xiaokele Cu (Mo) (ca. 150 Ma; [5]) deposits.

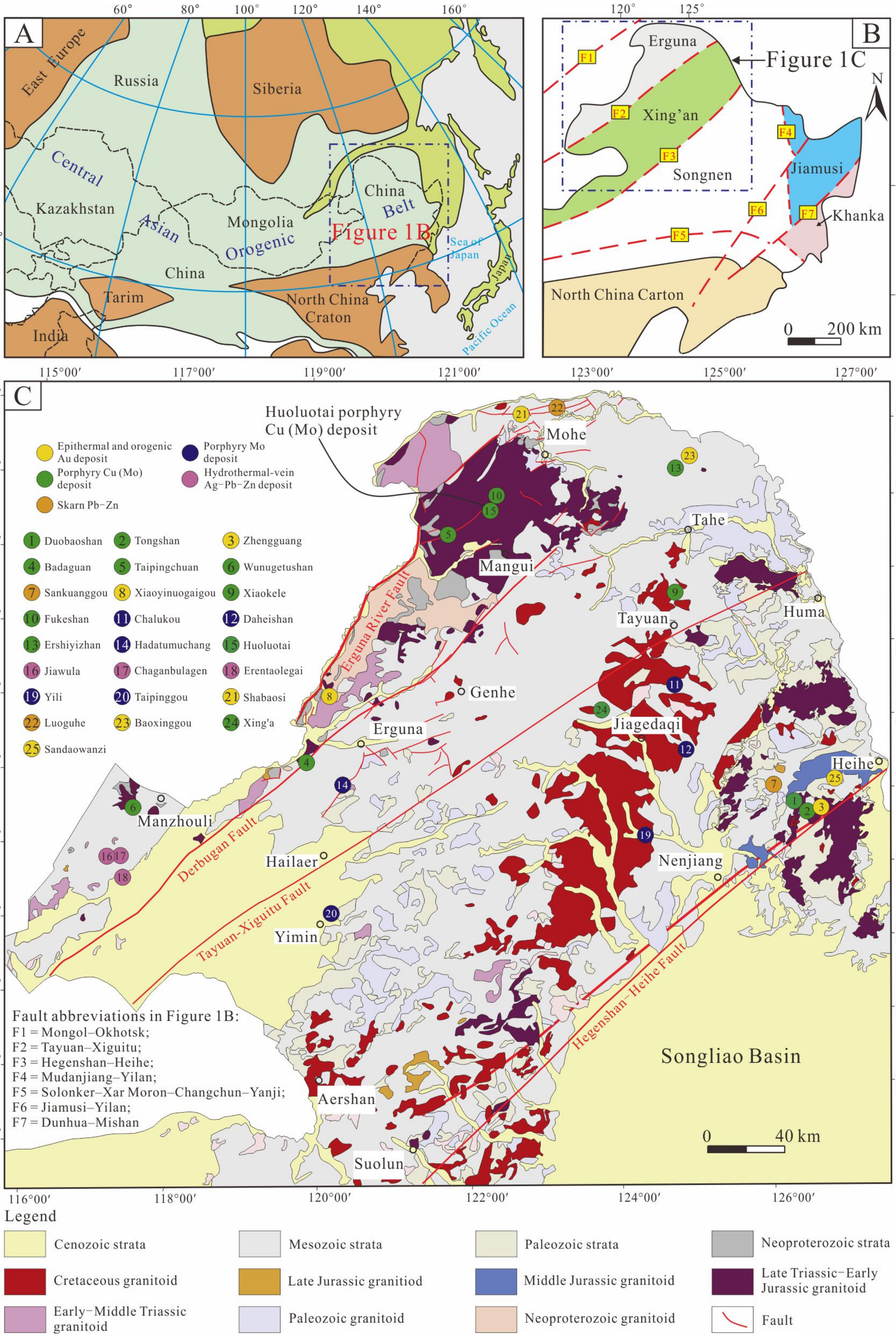

Figure 1. (**A**) Location of the CAOB [6]. (**B**) Geological map of NE China [7]. (**C**) Geological map of the NGXR (modified from [3]).

The Huoluotai Cu (Mo) deposit, which is located in the NGXR, contains estimated industrial metal resources of >4900 t Cu and >300 t Mo and is currently being explored [8]. Previous studies have focused on the geological characteristics [9], geochronology [9,10], and geochemistry of the igneous rocks in this deposit [11]. According to these studies, the Huoluotai Cu (Mo) deposit is considered to be a porphyry deposit. The magmatic activity of the Huoluotai Cu (Mo) deposit mainly occurred in the Late Jurassic–Early Cretaceous (ca. 150–140 Ma), and Cu (Mo) mineralization was closely related to the Late Jurassic granodiorite porphyry (ca. 149 Ma; [11]). Nevertheless, the lack of comprehensive research on the ore-forming fluids limits our understanding of the ore-forming conditions of the Huoluotai Cu (Mo) deposit. Three important issues have not been resolved: (1) the origin and detailed evolution of the ore-forming fluids are unknown; (2) the source of the ore-forming materials remains uncertain; and (3) the possible mineralization processes have not been determined.

To solve these problems, the present study presents micro-thermometry and laser Raman spectroscopy data of the fluid inclusions (FIs), and C–H–O–S–Pb isotope compositions. The results will provide new clues for further prospecting directions in the Huoluotai Cu (Mo) deposit, as well as the late Mesozoic porphyry Cu deposits in the NGXR.

2. Regional Geology

From west to east, NE China is divided into the Erguna, Xing’an, Songnen, Jiamusi, and Khanka blocks (Figure 1B; [12]). The NGXR is located in the western part of NE China, including the Erguna Block, the northern part of the Xing’an Block, and the northwestern part of the Songnen Block (Figure 1B; [13]). The Huoluotai Cu (Mo) deposit is located in the northern segment of the Erguna Block (Figure 1C). The Erguna Block collided with the Xing’an Block along the Tayuan–Xiguitu suture at ca. 500 Ma (Figure 1C; [14,15]). The main faults in the Erguna Block are NE-striking Erguna and Derbugan River faults (Figure 1C; [16]). The basement of the Erguna Block mainly contains Neoproterozoic granitoids and metamorphic supracrustal rocks [16–19]. The exposed strata in the Erguna Block mainly consist of Paleozoic marine sediments [20], widely distributed Mesozoic terrigenous clastic rocks, and volcanic rocks [21]. Magmatism in the NGXR can be divided into Paleozoic, Early–Middle Triassic, Late Triassic–Early Jurassic, Middle–Late Jurassic, and Cretaceous (Figure 1C; [12,22–24]).

3. Ore Deposit Geology

The Huoluotai porphyry Cu (Mo) deposit is located ~50 km southwest of Mohe City, Heilongjiang Province (Figure 1C). The NNW-striking Huoluotai River Fault is distributed in the northeastern part of the district (Figure 2A). Multiperiod igneous rocks developed in the Huoluotai ore district (Figure 2). The Early Jurassic medium–fine-grained monzogranite (ca. 180 Ma) was intruded by Late Jurassic granodiorite porphyry (ca. 149 Ma), diorite porphyry (ca. 146 Ma), and Early Cretaceous granite porphyry dikes (ca. 142 Ma) (Figure 2; [11]). The quartz diorite porphyry dikes intruded into the granodiorite porphyry (Figure 2B). Mineralization developed around the granodiorite porphyry (Figure 2B), and 66 orebodies have been identified. These orebodies are characterized by disseminations, veinlets, and stockworks and are generally 1–9 m thick, dipping toward the east at angles of 20–35°. In the dipping direction, the explored orebodies usually extend downward for 50–240 m.

Three types of alteration were identified in the Huoluotai Cu (Mo) deposit: potassic, chlorite–epidote, and phyllic alterations from early to late (Figure 3A–D). From center to edge, two alteration zones can be recognized: the potassic alteration zone and the phyllic alteration zone (Figure 2B). Hydrothermal alteration surrounds the granodiorite porphyry and is correlated strongly with the granodiorite porphyry (Figure 2B). Potassic alteration is characterized by secondary K-feldspar and biotite (Figure 3A,B). The ore minerals developed in the potassic alteration zone are mainly magnetite, chalcopyrite, hematite, and small amounts of molybdenite (Figure 3E–H). Magnetite mainly developed as disseminations and/or magnetite ± quartz ± chalcopyrite veinlets. Cu (Mo) orebodies mainly developed in the potassic alteration zone. Chalcopyrite mainly developed as disseminations, masses, or quartz + chalcopyrite veins in the potassic alteration zone (Figure 3G,H). Potassic alteration was locally overprinted by epidote and chlorite alterations. Phyllic alteration can be distinguished by secondary sericite and quartz (Figure 3C,D). The ore minerals present in the phyllic alteration zone are mainly pyrite, chalcopyrite, and molybdenite (Figure 3I). In the phyllic alteration zone, chalcopyrite occurs mainly as disseminations, while molybdenite occurs mainly as disseminations and/or quartz + molybdenite + pyrite ± chalcopyrite veins (Figure 3I).

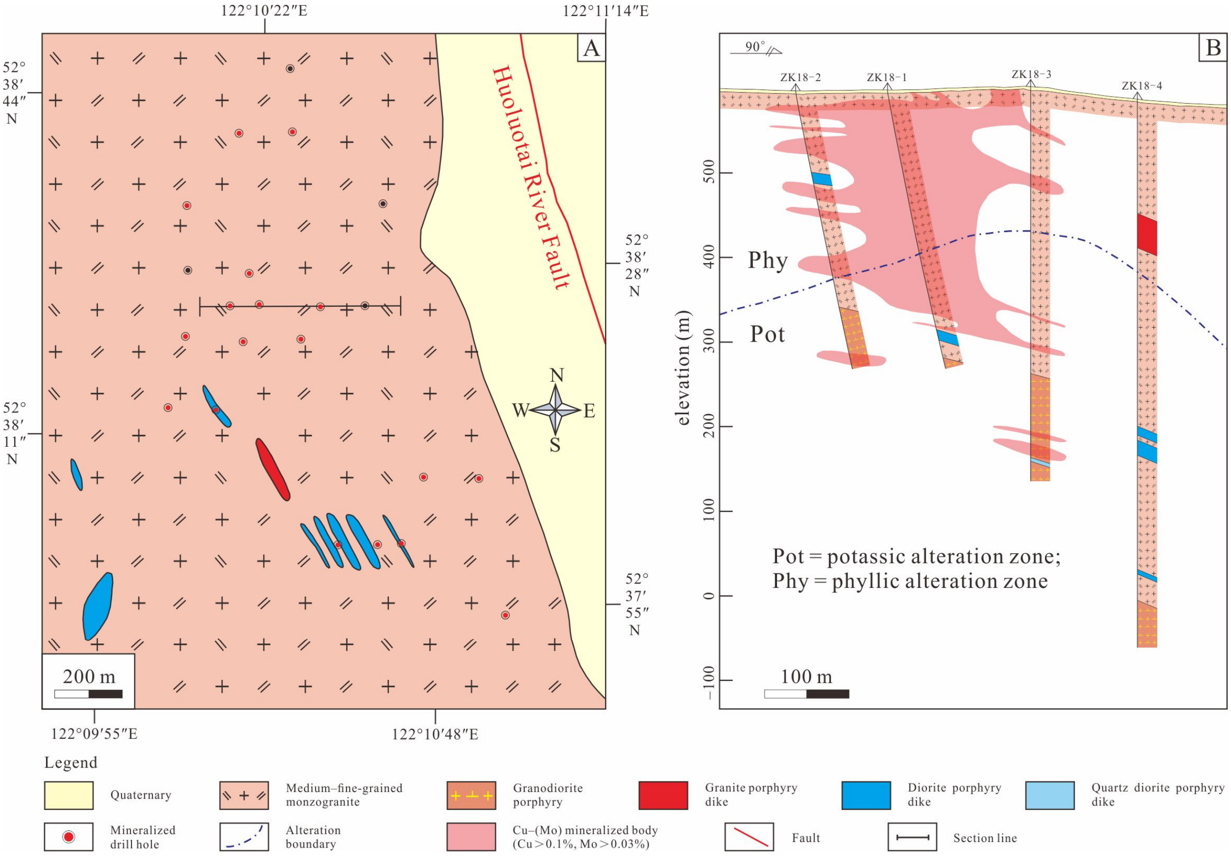

Figure 2. (**A**) Geological map of the Huoluotai Cu (Mo) deposit (modified from [8]). (**B**) Geological sections in the Huoluotai Cu (Mo) deposit (modified from [8]).

Based on the mineral assemblages and crosscutting relationships between veins in the Huoluotai Cu (Mo) deposit (Figure 3), four mineralization stages were identified: the sulfide-barren quartz stage (stage I), the quartz + chalcopyrite ± pyrite ± molybdenite stage (stage II), the quartz + polymetallic sulfide stage (stage III), and the quartz + calcite ± pyrite ± fluorite stage (stage IV) (Figure 4). Stage I is characterized by sulfide-barren quartz veins, which are rare and generally discontinuous (Figure 3E). There is no obvious cutting relationship between the veins in stage I and those in other mineralization stages. Stage I veins are mainly concentrated in the potassic alteration zone. Copper is mainly found in stage II. Stage II veins are generally continuous and irregular (Figure 3G) and mainly contain quartz, chalcopyrite, pyrite, and molybdenite. Stage II veins are distributed mainly in the potassic alteration zone. Stage III veins are generally continuous and straight (Figure 3I) and are characterized by quartz, pyrite, and molybdenite. Stage III veins are usually concentrated in the phyllic alteration zone. Stage IV veins are usually irregular and dominated by quartz and calcite (Figure 3J), with small amounts of fluorite. The sulfide observed in stage IV is only pyrite. Supergene mineralization is dominated by molybdite, azurite, and malachite (Figure 3K,L).

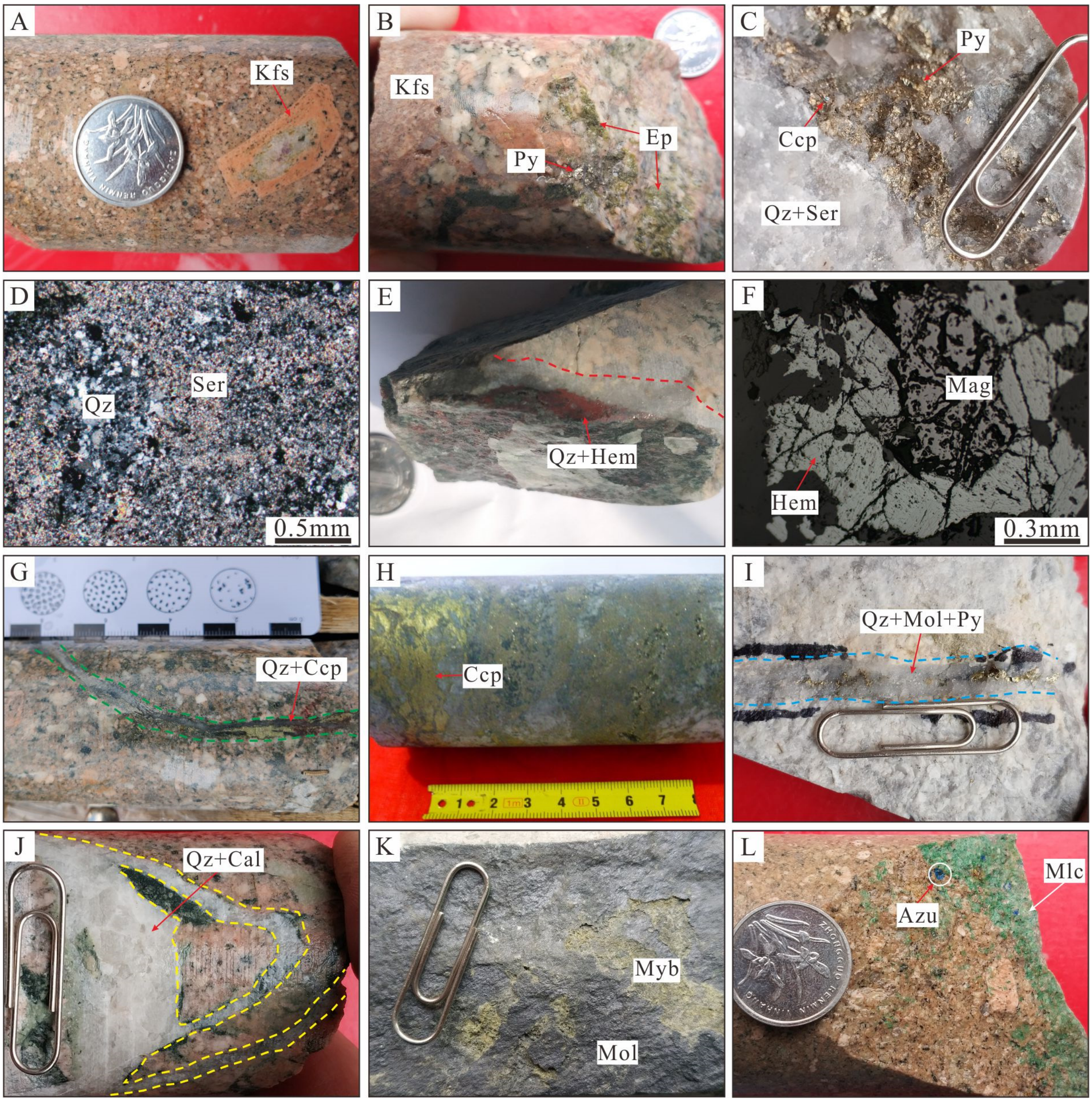

Figure 3. Photographs and photomicrographs of representative hydrothermal alterations and ore mineralization features in the Huoluotai Cu (Mo) deposit. (**A**) Potassic alteration observed in the granodiorite porphyry. (**B**) Potassic alteration overprinted by epidote alteration. (**C**) Phyllic alteration in the granodiorite porphyry. (**D**) Phyllic alteration characterized by an alteration assemblage of sericite and quartz. (**E**) Stage I quartz + hematite vein in potassic-altered granodiorite porphyry. (**F**) Anhedral hematite and magnetite in stage I. (**G**) Stage II quartz + chalcopyrite vein in potassic-altered granodiorite porphyry. (**H**) Dense disseminated chalcopyrite developed in the granodiorite porphyry. (**I**) Stage III quartz + molybdenite + pyrite vein in phyllic-altered wall rock. (**J**) Stage IV quartz + calcite vein in potassic-altered granodiorite porphyry. (**K**) Primary molybdenite oxidized to molybdite. (**L**) Primary chalcopyrite oxidized to azurite and malachite. Abbreviations: Qz = quartz; Kfs = K-feldspar; Ep = epidote; Ser = sericite; Cal = calcite; Mag = magnetite; Hem = hematite; Py = pyrite; Ccp = chalcopyrite; Mol = molybdenite; Myb = molybdite; Mlc = malachite; Azu = azurite.

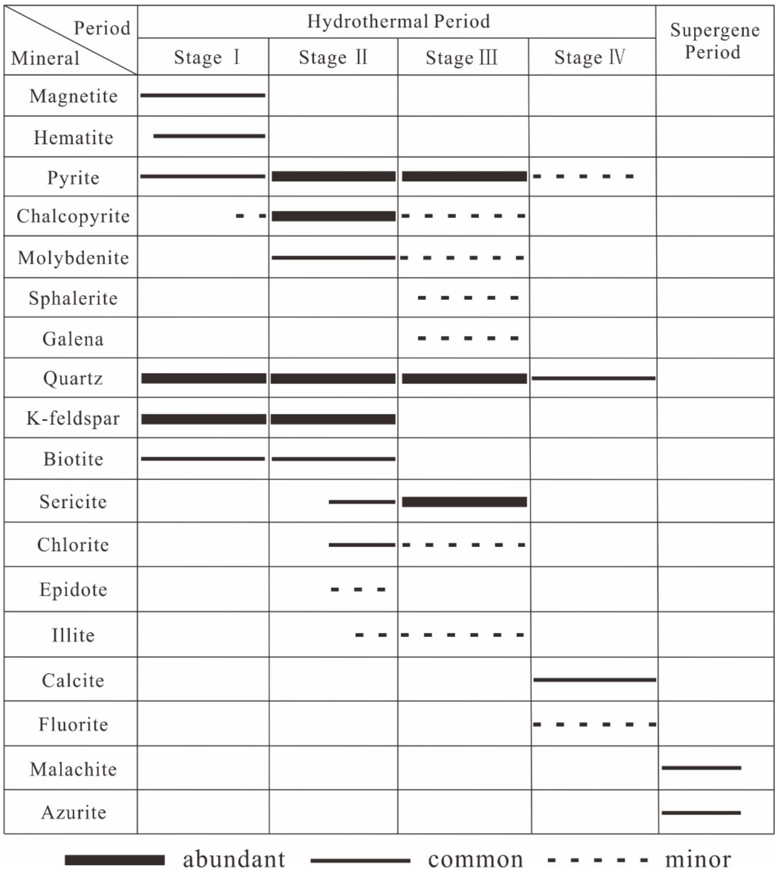

Figure 4. Paragenetic sequence of the major minerals in the Huoluotai Cu (Mo) deposit.

4. Analytical Methods

4.1. Fluid Inclusion Measurements

In total, 31 quartz samples were used to perform FI measurements at the Key Laboratory of Mineral Resources Evaluation in Northeast Asia, Ministry of Land and Resources, Changchun, China. Secondary FIs were not analyzed [25]. All types of FIs were selected for laser Raman spectra analyses using an RM-2000 Laser Raman microprobe. Microthermometric analyses were performed using a Linkam THMS-600 heating–freezing stage (Linkam Scientific Instruments Ltd., Epsom, UK).

4.2. H–O Isotope Analyses

Six quartz samples were selected for H–O isotope analysis at the Center of Analytical Laboratory in the Beijing Research Institute of Uranium Geology (BRIUG), China National Nuclear Corporation (Beijing, China). The H–O isotope compositions were analyzed by a Finnigan MAT253-EM mass spectrometer. The O and H isotope compositions were analyzed using the conventional BrF_5 method and the Zn reduction method, respectively [26,27]. The H–O isotope values were normalized with the Vienna Standard Mean Ocean Water (V-SMOW) standards. The analytical precision was better than 0.2‰ for $\delta^{18}O$ and 2‰ for δD.

4.3. C–O Isotope Analyses

Four representative calcite samples were selected for C–O isotope analysis at BRIUG. The C–O isotope analyses of calcite were performed using the 100% phosphoric acid method [28] with a MAT-251EM mass spectrometer. $\delta^{13}C$ used the Pee Dee Belemnite (PDB) standard, and $\delta^{18}O$ used the SMOW standard. The analytical precision was better than 0.1‰ for $\delta^{13}C$ and 0.2‰ for $\delta^{18}O$.

4.4. S–Pb Isotope Analyses

The S isotope compositions of seven representative sulfide samples were analyzed at BRIUG. The values of $\delta^{34}S$ for the sulfide samples were determined on SO_2 produced by the reaction between the sulfide and cuprous oxide. $\delta^{34}S$ used the Vienna Cañon Diablo Troilite (V-CDT) standard. The Pb isotope compositions of four representative sulfide samples were also analyzed at BRIUG. Sulfide samples were dissolved in a mixed solution of HF + HNO_3 at 150 °C for seven days. The Pb isotope compositions were measured using a MAT-261 thermal ionization mass spectrometer.

5. Analytical Results

5.1. Fluid Inclusions

5.1.1. Microscopy Investigations of Fluid Inclusions

According to the phases, filling degree, and combination relationship of FIs at a normal temperature (25 °C), four different FI types were identified in the quartz samples from the Huoluotai Cu (Mo) deposit, as described below.

Liquid-rich (L-type) FIs are most common in four mineralization stages, which consist of two phases with $V_{H_2O}/(V_{H_2O} + L_{H_2O}) < 50$ vol.% at ~25 °C (Figure 5A,C–E,G–I). The vapor phase accounts for 10–20 vol.% of the FI volume. The FIs range from 3 to 20 μm in size and are round or irregular in shape. Commonly, L-type FIs homogenize into liquid during heating.

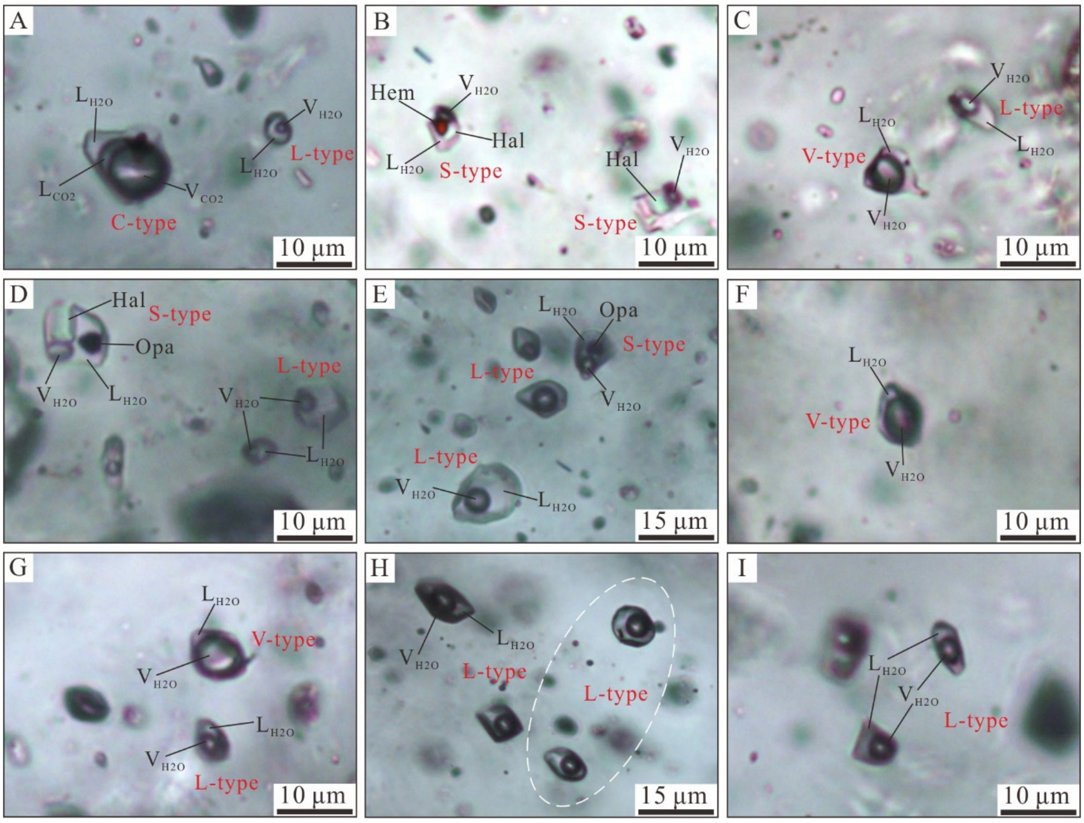

Figure 5. Photomicrographs of the representative primary FIs in four mineralization stages from the Huoluotai Cu (Mo) deposit. (**A**) The coexistence of primary L- and C-type FIs in stage I quartz. (**B**) S-type FIs with hematite and/or halite daughter minerals in stage I quartz. (**C**) The coexistence of primary L- and V-type FIs in stage I quartz. (**D**,**E**) The coexisting S- and L-type FIs in stage II quartz. (**F**) Primary V-type FIs in stage II quartz. (**G**) The coexisting L- and V-type FIs in stage III quartz. (**H**) Primary L-type FIs in stage III quartz. (**I**) Primary L-type FIs in stage IV quartz. Abbreviations: L_{H_2O} = H_2O liquid; V_{H_2O} = H_2O vapor; L_{CO_2} = CO_2 liquid; V_{CO_2} = CO_2 vapor; Hal = halite; Hem = hematite; Opa = unidentified opaque mineral.

Vapor-rich (V-type) FIs were identified in stages I, II, and III but absent in stage IV. These FIs consist of two phases with $V_{H_2O}/(V_{H_2O} + L_{H_2O}) > 50$ vol.% at ~25 °C and have 60–90 vol.% vapor bubbles (Figure 5C,F,G). These FIs are normally round or oval in shape and range in size from 5 to 20 μm. Commonly, V-type FIs homogenize into vapor during heating.

Daughter-mineral-bearing three-phase (S-type) FIs were detected in stages I and II. S-type FIs consist of an aqueous liquid, a vapor bubble, and one or more solid daughter minerals at ~25 °C (Figure 5B,D,E). These FIs are normally oval or irregular in shape and range from 5 to 20 μm in size. Additionally, these FIs may contain one, two, or three daughter minerals, which can be halite or ore minerals (Figure 5B,D,E). The halites are mainly transparent, pale white, and cubic in shape (Figure 5B,D). The ore minerals are opaque (Figure 5B,D,E). Most halites dissolved after the vapor-bubble disappeared during heating.

CO_2-bearing (C-type) FIs only occur in stage I. These FIs are normally round, oval, or irregular in shape and range from 8 to 15 μm in size. Most C-type FIs consist of three phases ($L_{H_2O} + L_{CO_2} + V_{CO_2}$), and occasionally two phases ($L_{H_2O} + L_{CO_2}$) at ~25 °C. The latter changes into three phases with the appearance of CO_2 bubbles at ~10 °C. Most C-type FIs have 50–70 vol.% CO_2 volumetric proportions $[(V_{CO_2} + L_{CO_2})/(V_{CO_2} + L_{CO_2} + L_{H_2O})]$ at ~25 °C (Figure 5A), and can be homogenized into a liquid CO_2 phase.

5.1.2. Micro-Thermometric Results

FI micro-thermometric data in this study are listed in Table 1 and shown in Figure 6. The salinities of L- and V-type FIs were estimated according to the HOKIEFLINCS_H_2O–NaCl program [29]. The salinities of S-type FIs were calculated using the equations from [30]. We calculated the salinities of C-type FIs based on the melting temperatures of CO_2 clathrate in the H_2O–CO_2–NaCl system [31].

Table 1. Micro-thermometric data and calculated parameters for FIs from the Huoluotai Cu (Mo) deposit.

Mineralized Stages	Host Minerals	FI Types	N	$T_{m\text{-}CO2}$ (°C)	$T_{m\text{-}cla}$ (°C)	$T_{h\text{-}CO2}$ (°C)	$T_{h\text{-}total}$ (°C)	$T_{m\text{-}ice}$ (°C)	$T_{h\text{-}s}$ (°C)	$T_{h\text{-}v}$ (°C)	Salinity (wt.% NaCl Equivalent)
I	Quartz	L-type	32	/	/	/	/	−8.1 to −4.5	/	406–479	7.2–11.8
		V-type	12	/	/	/	/	−7.9 to −5.8	/	427–471	8.9–11.6
		S-type	20	/	/	/	/	/	424–485	/	50.1–57.8
		C-type	8	−57.4 to −56.8	3.5–5.5	28.2–30.5	429–470	/	/	/	8.3–11.3
II	Quartz	L-type	34	/	/	/	/	−6.6 to −3.1	/	307–398	5.1–10.0
		V-type	14	/	/	/	/	−6.4 to −3.8	/	326–396	6.2–9.7
		S-type	17	/	/	/	/	/	356–414	/	43.0–48.9
III	Quartz	L-type	47	/	/	/	/	−4.5 to −0.9		223–336	1.6–7.2
		V-type	16	/	/	/	/	−3.6 to −1.8	/	265–332	3.1–5.9
IV	Quartz	L-type	40	/	/	/	/	−2.6 to −0.7		143–249	1.2–4.3

Abbreviations: $T_{h\text{-}v}$ = homogenization temperature of vapor-rich or liquid-rich fluid inclusions; $T_{h\text{-}s}$ = dissolution temperature of halite; $T_{m\text{-}ice}$ = temperature of final ice melting; $T_{h\text{-}total}$ = total homogenization temperature of CO_2 fluid inclusions; $T_{h\text{-}CO_2}$ = homogenization temperature of the CO_2 phases; $T_{m\text{-}cla}$ = final melting temperature of CO_2–H_2O clathrate; $T_{m\text{-}CO_2}$ = final melting temperature of solid CO_2.

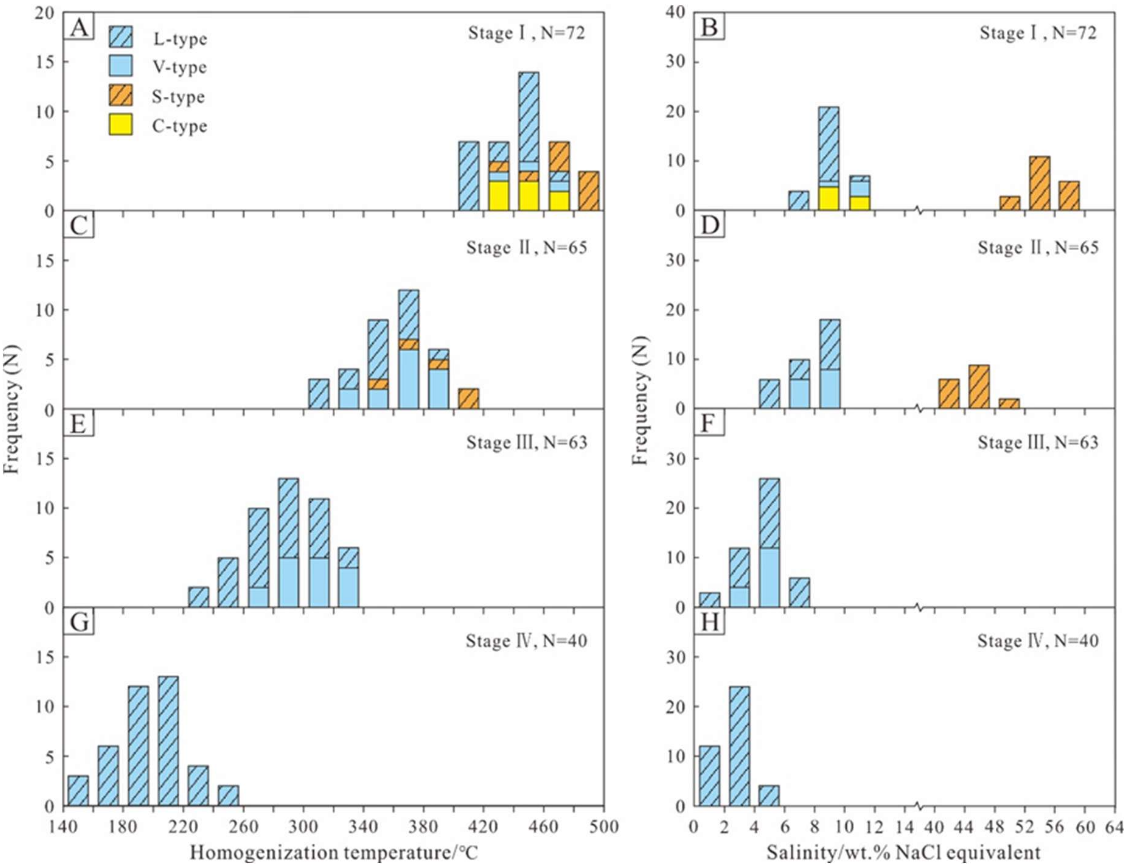

Figure 6. Frequency histograms of the total homogenization temperatures (Th) and salinities of FIs (wt.% NaCl equivalent) in four mineralization stages from the Huoluotai Cu (Mo) deposit. (**A**) Homogenization temperatures histogram for L-, V-, S-, and C-type FIs from stage I quartz; (**B**) Salinities histogram for L-, V-, S-, and C-type FIs from stage I quartz; (**C**) Homogenization temperatures histogram for L-, V-, and S-type FIs from stage II quartz; (**D**) Salinities histogram for L-, V-, and S-type FIs from stage II quartz; (**E**) Homogenization temperatures histogram for L- and V-type FIs from stage III quartz; (**F**) Salinities histogram for L- and V-type FIs from stage III quartz; (**G**) Homogenization temperatures histogram for L-type FIs from stage IV quartz; (**H**) Salinities histogram for L-type FIs from stage IV quartz.

Stage I (quartz): L-, V-, S-, and C-type FIs were observed in stage I quartz (Figure 5A–C). The L-type FIs homogenized into the aqueous liquid phase at 406–479 °C (peaking at 440–460 °C, n = 32) (Figure 6A) during heating. These FIs yielded final ice-melting temperatures ($T_{m\text{-}ice}$) of −8.1 to −4.5 °C, with calculated salinities of 7.2–11.8 wt.% NaCl equivalent (peaking at 8–10 wt.% NaCl equivalent, n = 32) (Figure 6B). The V-type FIs homogenized into the vapor phase at 427–471 °C (n = 12; Figure 6A). These V-type FIs yielded final ice-melting temperatures ($T_{m\text{-}ice}$) of −7.9 to −5.8 °C, corresponding to salinities of 8.9–11.6 wt.% NaCl equivalent (n = 12; Figure 6B). During heating, all S-type FIs commonly homogenized into the aqueous liquid phase, with halite daughter minerals dissolving at temperatures ($T_{h\text{-}s}$) varying from 424 to 485 °C (n = 20; Figure 6A), with calculated salinities of 50.1–57.8 wt.% NaCl equivalent (peaking at 52–56 wt.% NaCl equivalent, n = 20) (Figure 6B). C-type FIs were completely homogenized into liquid H_2O at temperatures ($T_{h\text{-}total}$) of 429–470 °C (n = 8) (Figure 6A). These FIs yielded initial melting temperatures ($T_{m\text{-}CO2}$) of solid CO_2 from −57.4 to −56.8 °C and clathrate melting temperatures ($T_{m\text{–}cla}$) from 3.5 to 5.5 °C, corresponding to salinities of 8.3–11.3 wt.% NaCl equivalent (n = 8) (Figure 6B). The CO_2 phase homogenized into the liquid CO_2 phase at temperatures ($T_{h\text{-}CO_2}$) of 28.2–30.5 °C.

Stage II (quartz): L-, V-, and S-type FIs were observed in stage II quartz (Figure 5D–F). The L-type FIs homogenized into the aqueous liquid phase at 307–398 °C (peaking at 340–380 °C, n = 34) (Figure 6C) during heating. These FIs yielded final ice-melting temperatures ($T_{\text{m-ice}}$) of −6.6 to −3.1 °C, with calculated salinities of 5.1–10.0 wt.% NaCl equivalent (peaking at 8–10 wt.% NaCl equivalent, n = 34) (Figure 6D). V-type FIs homogenized into the vapor phase at 326–396 °C (n = 14; Figure 6C). These V-type FIs yielded final ice-melting temperatures ($T_{\text{m-ice}}$) of −6.4 to −3.8 °C, corresponding to salinities of 6.2–9.7 wt.% NaCl equivalent (n = 14) (Figure 6D). During heating, all S-type FIs commonly homogenized into the aqueous liquid phase, with the halite daughter minerals dissolving at temperatures ($T_{\text{h-s}}$) varying from 356 to 414 °C (peaking at 360–400 °C, n = 17) (Figure 6C), with calculated salinities of 43.0–48.9 wt.% NaCl equivalent (n = 17; Figure 6D).

Stage III (quartz): L- and V-type FIs are widespread in stage III quartz (Figure 5G,H). The L-type FIs homogenized into the aqueous liquid phase at 223–336 °C (peaking at 280–320 °C, n = 47) (Figure 6E) and yielded final ice-melting temperatures ($T_{\text{m-ice}}$) of –4.5 to –0.9 °C, with calculated salinities of 1.6–7.2 wt.% NaCl equivalent (peaking at 4–6 wt.% NaCl equivalent, n = 47) (Figure 6F). The V-type FIs homogenized into the vapor phase at 265–332 °C (n = 16; Figure 6E). These V-type FIs yielded final ice-melting temperatures ($T_{\text{m-ice}}$) of −3.6 to −1.8 °C, corresponding to salinities of 3.1–5.9 wt.% NaCl equivalent (n = 16) (Figure 6F).

Stage IV (quartz): Only the L-type FIs were recognized in stage IV quartz (Figure 5I). The L-type FIs homogenized into the aqueous liquid phase at 143–249 °C (peaking at 180–220 °C, n = 40) (Figure 6G) and yielded final ice-melting temperatures ($T_{\text{m-ice}}$) of −2.6 to −0.7 °C, with calculated salinities of 1.2–4.3 wt.% NaCl equivalent (peaking at 2–4 wt.% NaCl equivalent, n = 40) (Figure 6H).

5.1.3. Laser Raman Spectroscopy

The gas phase composition of some representative FIs in the four mineralization stages were selected for laser Raman spectroscopy analysis. Representative laser Raman spectra are shown in Figure 7. C-type FIs in stage I were universally found to be rich in CO_2 (Figure 7A). Vapor phases of the V-type FIs in stages I, II, and III only contained H_2O (Figure 7B). L-type FIs in the four mineralization stages only contained H_2O (Figure 7C,D). These analytical results suggest that the ore-forming fluids of stage I represent an H_2O–CO_2–NaCl system that transforms into an H_2O–NaCl system from stages II to IV.

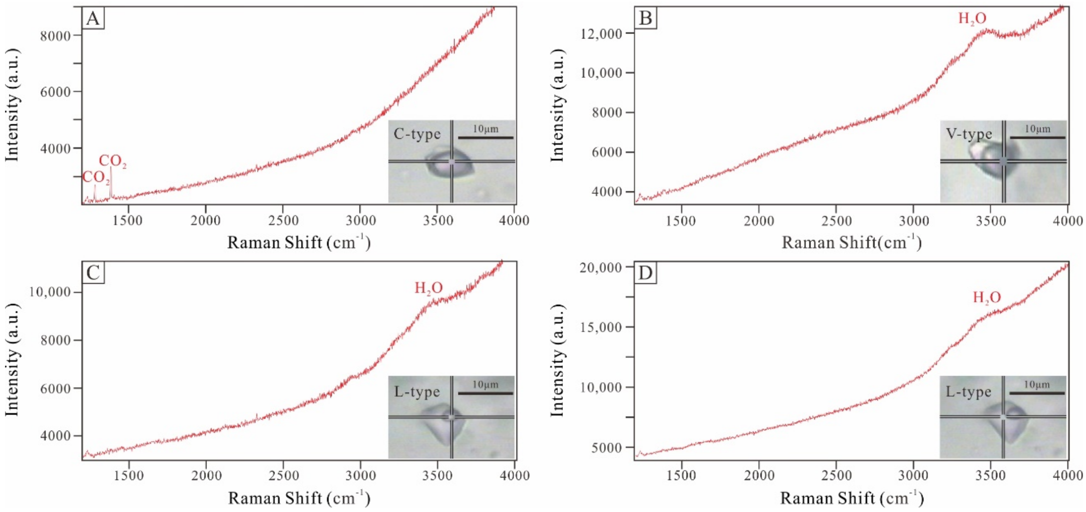

Figure 7. Representative laser Raman spectra for different types of FIs from the Huoluotai Cu (Mo) deposit. (**A**) The vapor phases of C-type FIs in stage I are rich in CO_2; (**B**) The vapor phases of V-type FIs are almost entirely H_2O; (**C**) The vapor phases of L-type FIs are almost entirely H_2O; (**D**) The liquid phases of L-type FIs are almost entirely H_2O.

5.2. H–O Isotopes

The H–O isotope results are listed in Table 2 and illustrated in Figure 8. Here, the $\delta^{18}O_{V\text{-}SMOW}$ values of the six quartz samples from the four mineralization stages range from 7.5 to 9.6‰. The $\delta^{18}O_{H_2O}$ values were calculated by the quartz–water equilibrium function [32], with the peak homogenization temperatures of FIs in the same mineralization stage. The calculated $\delta^{18}O_{H_2O}$ values for stages I, II, III, and IV are 6.5‰, 3.0‰ to 3.5‰, 0.2‰ to 1.9‰, and −2.5‰, respectively (Figure 8). The δD values for stages I, II, III, and IV are −108.1‰, −126.2‰ to −122.5‰, −132.9‰ to −130.9‰, and −139.1‰, respectively (Figure 8).

Table 2. H and O isotope data of quartz samples from the Huoluotai Cu (Mo) deposit.

Sample No.	Mineralized Stages	Mineral	$\delta^{18}O_{V\text{-}SMOW}$ (‰)	T (°C)	$\delta^{18}O_{H_2O}$ (‰)	δD (‰)
HLT-ZK18-2-HO1	I	Quartz	9.6	450	6.5	−108.1
HLT-ZK18-1-HO1	II	Quartz	8.3	370	3.5	−126.2
HLT-ZK18-1-HO2	II	Quartz	7.8	370	3.0	−122.5
HLT-ZK18-1-HO3	III	Quartz	7.5	290	0.2	−132.9
HLT-ZK18-2-HO2	III	Quartz	9.2	290	1.9	−130.9
HLT-ZK18-3-HO1	IV	Quartz	9.2	200	−2.5	−139.1

$\delta^{18}O_{H_2O}$ of water in equilibrium with quartz were calculated according to the equation of $1000\ln\alpha_{quartz\text{–}water} = 3.38 \times 10^6/T^2 - 3.4$ [32], which were defined by the peak homogenization temperatures (T) of FIs for corresponding quartz samples.

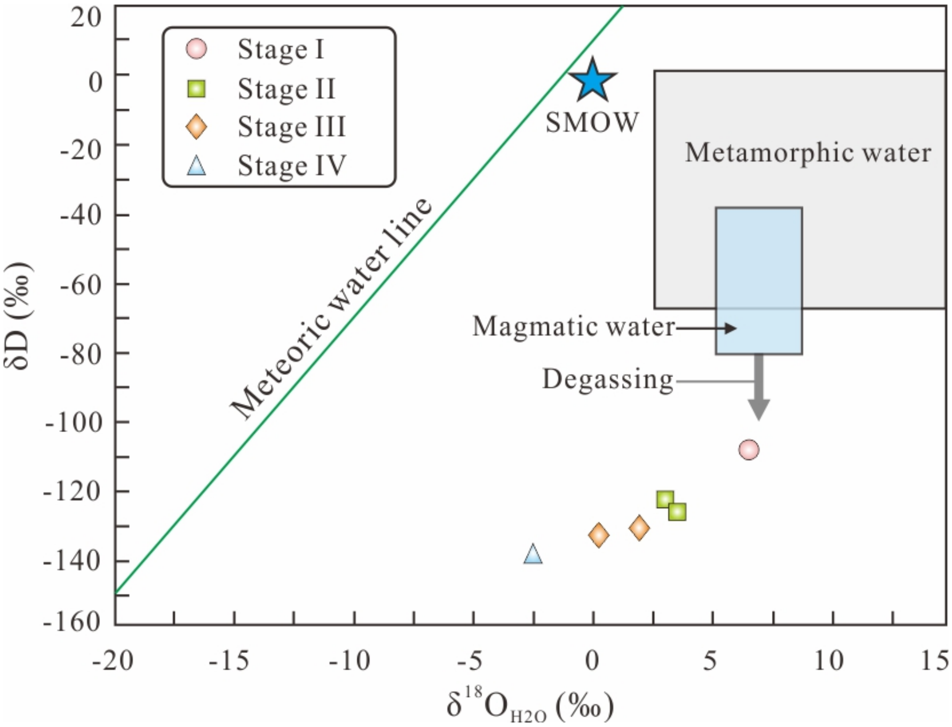

Figure 8. Plot of δD vs. $\delta^{18}O_{H_2O}$ for the ore-forming fluids in the Huoluotai Cu (Mo) deposit [33]. SMOW = Standard Mean Ocean Water.

5.3. C–O Isotopes

The C–O isotope results for the calcites in stage IV are listed in Table 3 and illustrated in Figure 9. Here, the $\delta^{13}C_{PDB}$ values of the four calcite samples in stage IV range from −3.1‰ to −0.2‰. The $\delta^{18}O_{SMOW}$ values range from 6.6‰ to 8.1‰.

Table 3. C and O isotope data of calcite samples from the Huoluotai Cu (Mo) deposit.

Sample No.	Mineral	Mineralized Stages	Sample Description	$\delta^{13}C_{PDB}$ (‰)	$\delta^{18}O_{PDB}$ (‰)	$\delta^{18}O_{SMOW}$ (‰)
HLT-ZK18-2-CO1	Calcite	IV	Qz+Cal+Py vein	−0.2	−22.1	8.1
HLT-ZK18-1-CO1	Calcite	IV	Qz+Cal+Py vein	−2.3	−22.8	7.4
HLT-ZK18-3-CO1	Calcite	IV	Qz+Cal+Py vein	−3.1	−23.5	6.6
HLT-ZK18-3-CO2	Calcite	IV	Qz+Cal+Py vein	−0.2	−23.3	6.9

$\delta^{18}O_{SMOW} = 1.03086 \times \delta^{18}O_{V\text{-}PDB} + 30.86$ [34].

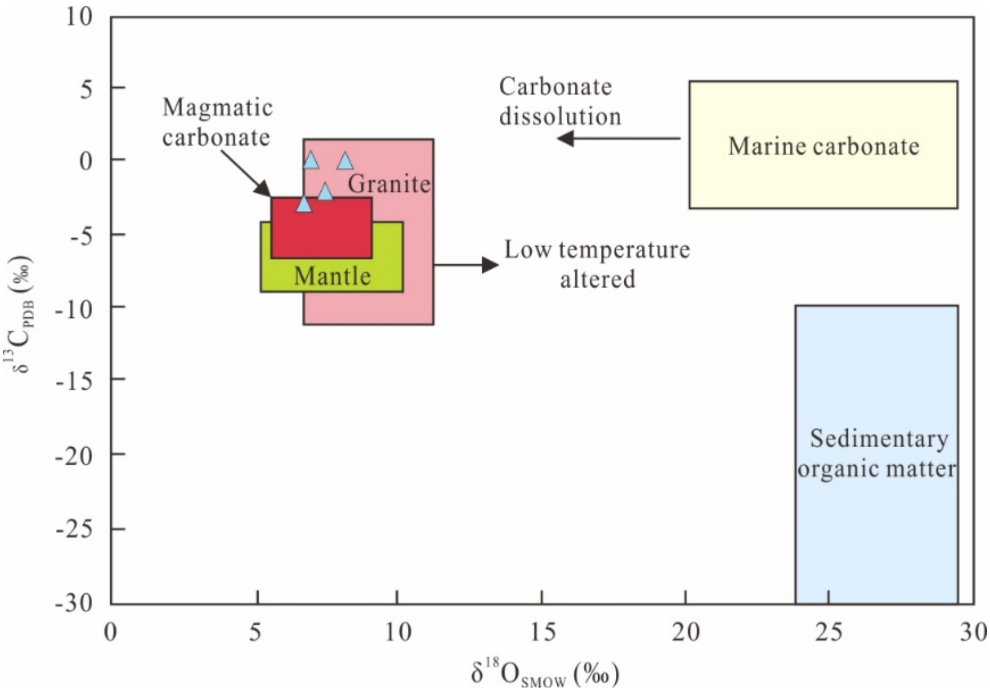

Figure 9. Plot of $\delta^{13}C_{PDB}$ vs. $\delta^{18}O_{SMOW}$ for the calcite from the Huoluotai Cu (Mo) deposit. The three main carbon sources include marine carbonate [35], sedimentary organic matter carbon [36], and magma-mantle carbonate [37].

5.4. S–Pb Isotopes

The S isotope results of the seven sulfide samples from the Huoluotai Cu (Mo) deposit are presented in Table 4 and plotted in Figure 10. The $\delta^{34}S_{V\text{–}CDT}$ values of the seven sulfides range from 0.2‰ to 3.7‰ (average = 1.9‰) (Table 4; Figure 10).

Table 4. S isotope data of sulfide samples from the Huoluotai Cu (Mo) deposit.

Sample No.	Mineral	Mineralized Stages	Sample Description	δ^{34}SV–CDT (‰)
HLT-ZK18-1-S1	Pyrite	I	Qz+Hem+Py vein	2.8
HLT-ZK18-1-S2	Pyrite	I	Qz+Kfs+Py vein	2.3
HLT-ZK18-2-S1	Chalcopyrite	II	Qz+Kfs+Ccp vein	1.8
HLT-ZK18-1-S3	Pyrite	II	Qz+Kfs+Ccp+Py vein	1.4
HLT-ZK18-1-S4	Chalcopyrite	III	Qz+Ser+Ccp+Py vein	0.2
HLT-ZK18-2-S2	Molybdenite	III	Qz+Ser+Mol vein	3.7
HLT-ZK18-3-S1	Pyrite	IV	Qz+Cal+Py vein	1.4

Abbreviations: Qz = quartz; Kfs = K-feldspar; Ser = sericite; Cal = calcite; Hem = hematite; Ccp = chalcopyrite; Mol = molybdenite; Py = pyrite.

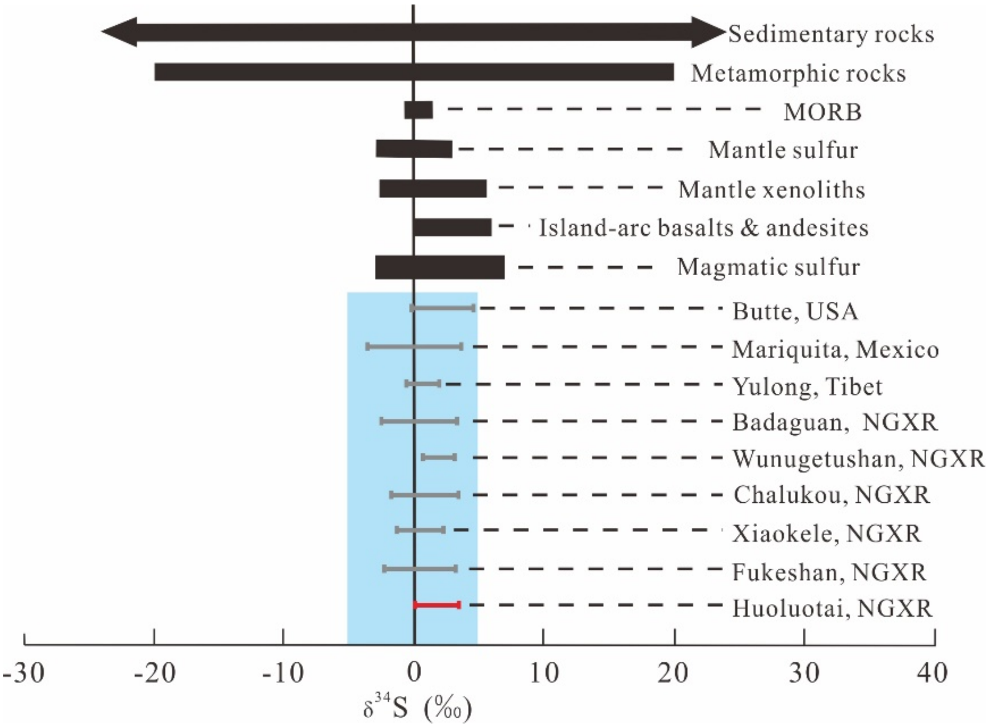

Figure 10. S isotope compositions of sulfides from the Huoluotai Cu (Mo) deposit, important S reservoirs [38–40], and other typical porphyry deposits elsewhere in the world [4,5,41–46].

The Pb isotope compositions of the four sulfide samples from the Huoluotai Cu (Mo) deposit are listed in Table 5 and illustrated in Figure 11. Here, the Pb isotope compositions of sulfides have a limited variation in $^{206}Pb/^{204}Pb$, $^{207}Pb/^{204}Pb$, and $^{208}Pb/^{204}Pb$, varying from 18.352 to 18.435, 15.552 to 15.578, and 38.212 to 38.309, respectively.

Table 5. Pb isotope data of sulfide samples from the Huoluotai Cu (Mo) deposit.

Sample No.	Mineral	Mineralized Stages	Sample Description	$^{206}Pb/^{204}Pb$	Error	$^{207}Pb/^{204}Pb$	Error	$^{208}Pb/^{204}Pb$	Error
HLT-ZK18-1-Pb1	Pyrite	I	Qz+Kfs+Py vein	18.409	0.003	15.564	0.002	38.255	0.005
HLT-ZK18-1-Pb2	Chalcopyrite	II	Qz+Ccp vein	18.352	0.002	15.552	0.002	38.212	0.005
HLT-ZK18-2-Pb1	Pyrite	III	Qz+Mol+Py vein	18.435	0.002	15.571	0.002	38.284	0.005
HLT-ZK18-1-Pb3	Pyrite	III	Qz+Mol+Py vein	18.428	0.001	15.578	0.001	38.309	0.003

Abbreviations: Qz = quartz; Kfs = K-feldspar; Ccp = chalcopyrite; Mol = molybdenite; Py = pyrite.

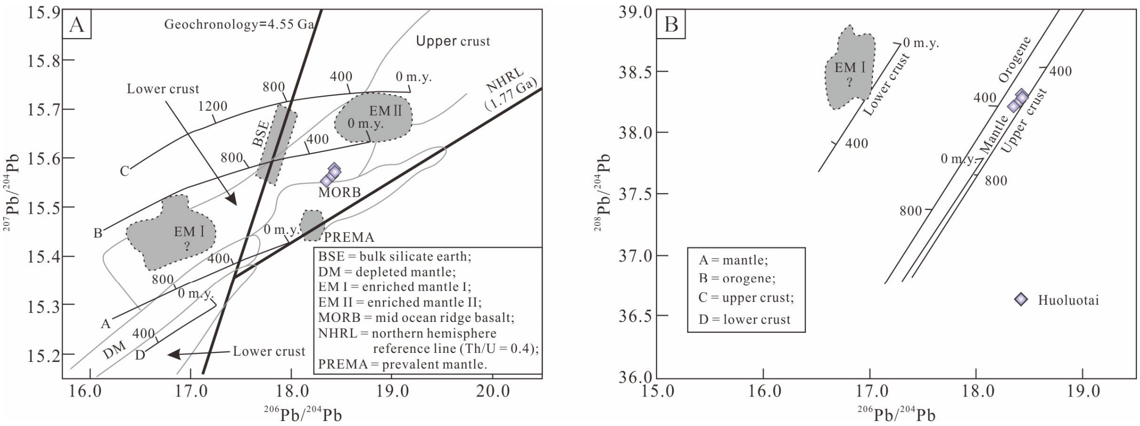

Figure 11. Pb isotope compositions of sulfides from the Huoluotai Cu (Mo) deposit [47]. (**A**) $^{207}Pb/^{204}Pb$ vs. $^{206}Pb/^{204}Pb$. (**B**) $^{208}Pb/^{204}Pb$ vs. $^{206}Pb/^{204}Pb$.

6. Discussion

6.1. Source of the Ore-forming Materials

The $\delta^{34}S_{V\text{–}CDT}$ values (0.2‰ to 3.7‰) of the seven sulfides from the Huoluotai Cu (Mo) deposit overlap those of typical porphyry deposits in the NGXR, such as the Badaguan (–2.4‰ to 3.5‰; [45]), the Chalukou (–1.9‰ to 3.6‰; [43]), the Xiaokele (–1.2‰ to 2.4‰; [5]), and the Fukeshan (–2.3‰ to 3.4‰; [4]) deposits (Figure 10). These values are also consistent with the $\delta^{34}S_{V\text{–}CDT}$ values of typical porphyry deposits elsewhere in the world (−5‰ to 5‰; [39]). The $\delta^{34}S_{V\text{–}CDT}$ values of sulfide minerals for all these deposits fall into the magmatic sulfur range and are similar to those of mantle-derived sulfur (Figure 10; [39]). The Pb isotope compositions of sulfide minerals from the Huoluotai Cu (Mo) deposit are similar and homogeneous, indicating that they share a common Pb reservoir. In the ^{207}Pb/^{204}Pb vs. ^{206}Pb/^{204}Pb diagram (Figure 11A), Pb isotope data for the sulfide samples are plotted between the mantle and orogene evolution curves, near the mid-ocean ridge basalt (MORB) region. In the ^{208}Pb/^{204}Pb vs. ^{206}Pb/^{204}Pb diagram (Figure 11B), Pb isotope data are all plotted between the orogene and upper crust evolution curves (near the mantle evolution curve), showing the characteristics of a crust-mantle-mixing origin.

6.2. Estimation of Trapping Pressure

Trapping pressure can be estimated only when the actual trapping temperature is known or if fluid boiling occurred in the hydrothermal system at the time of entrapment [48,49]. During heating, L-type FIs homogenized into the aqueous liquid phase, while the V-type FIs homogenized into the vapor phase. In the Huoluotai Cu (Mo) deposit, the coexistence of L-, V-, and S-type FI assemblages (Figure 5A–F) within the same quartz crystal in stages I and II suggests that fluid boiling occurred in those stages. The trapping pressures in stage I were estimated to range from ~300 to ~500 bar (Figure 12A), assuming a simple NaCl–H_2O system using the isobar equations given in [50]. However, the addition of CO_2 to an NaCl–H_2O system could raise the solvus and increase the entrapment pressure (Figure 12B; [51–54]). Therefore, in this study, the estimated trapping pressures in stage I represent only the minimum values. The trapping pressures in stage II were estimated to be between ~100 and ~300 bar and were mostly concentrated around ~200 bar (Figure 12A) based on the isobar equations given in [50]. There are clear decreasing trends of pressure from stages I to II (Figure 12A). Fluid boiling did not occur in stages III and IV, so the estimated trapping pressures represent only the minimum values [54]. The minimum trapping pressures in stages III and IV were estimated to range from ~30 to ~150 bar and <50 bar, respectively (Figure 12A).

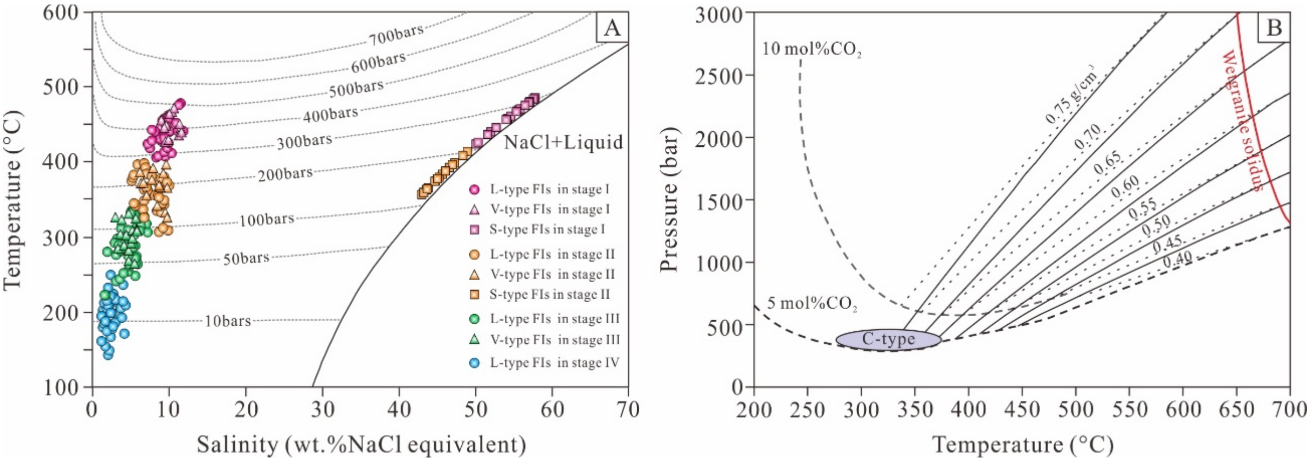

Figure 12. (**A**) Pressure estimation for FIs from the Huoluotai Cu (Mo) deposit. (**B**) Isochores for fluid of 4 wt.% NaCl, 5 mol% CO_2 (straight lines), and 10 mol% CO_2 (dashed lines). Data for the C-type FIs plot in the oval field.

6.3. Origin of the Ore-forming Fluids

The $\delta^{18}O_{H_2O}$ values for stage I (6.5‰) were close to those of magmatic water [55], indicating that the ore-forming fluids from stage I were derived from a magmatic source. The δD values for stage I were significantly lower than those for typical magmatic water (Figure 8; [56]). Previous studies have shown that the relatively depleted isotopic values of fluids could have been caused by water–rock interactions or magma degassing [57,58]. The depleted $\delta^{18}O_{H_2O}$ and δD isotopic characteristics were extensively recorded by fluids from an early stage in porphyry deposits of the NGXR [59], such as the Xiaokele Cu (Mo) (–1.2‰ to 2.4‰; [5]), the Fukeshan Cu (Mo) (–2.3‰ to 3.4‰; [4]), and the Chalukou Mo (–1.9‰ to 3.6‰; [43]) deposits, which were interpreted to be predominantly of magmatic origin. The δD and $\delta^{18}O_{H_2O}$ values for stages II, III, and IV were relatively lower than those for stage I and plotted in the region between the meteoric water line and the magmatic water field (close to the magmatic water field) (Figure 8), suggesting the involvement of some meteoric water but still dominated by magmatic water. In the $\delta^{13}C_{PDB}$ vs. $\delta^{18}O_{SMOW}$ diagram (Figure 9), the C–O isotope compositions of calcite in stage IV fell into the field of granite and magmatic carbonate, indicating that a certain amount of magmatic water was still involved in the mineralization process during the late mineralization stage.

6.4. Fluid Evolution and Mineralization Process

The occurrence of L-, V-, S-, and C-type FIs in stage I quartz indicates that the initial fluids belong to an H_2O–CO_2–NaCl system. These fluids are characterized by high homogenization temperatures and high salinities (Figure 6A,B). High amounts of hematite, magnetite (Figure 3E,F), and hematite-bearing S-type FIs (Figure 5B), but few sulfides, were found in stage I, suggesting that the initial fluids were highly oxidized [60,61]. This result is supported by the detection of oxidized gases (e.g., CO_2) in FIs via laser Raman spectroscopy analysis (Figure 7A). Sulfur in the magma was mostly present in the form of sulfate due to high oxygen fugacity and CO_2 activity [41,62], but sulfide mineralization would be inevitably constrained. These kinds of initial hydrothermal fluids were observed to be particularly prone to extensive potassic alterations and quartz + K-feldspar ± magnetite ± hematite ± pyrite veins in stage I.

Cu (Mo) mineralization occurred mainly in stage II. L-, V-, and S-type FIs were found in stage II quartz crystals (Figure 5D–F), which suggests that the ore-forming fluids of stage II belong to an H_2O–NaCl system. Hematite, magnetite, and C-type FIs were not found in stage II, suggesting that the CO_2 content and oxygen fugacity of the fluids were distinctly decreased compared to those in stage I. Such degassing of oxidized gas is considered to be a major process responsible for sulfate reduction [61]. This reduction in oxygen fugacity could be due to the escape of CO_2 caused by fluid boiling [63–65] and/or magnetite precipitation [66–68]. These results suggest that the fluid system only contained minor CO_2 in stage I, indicating that it is likely not a CO_2-rich system. Therefore, the immiscibility of CO_2 and water is not an important process in the Huoluotai Cu (Mo) deposit. The precipitation of magnetite was found to reduce S^{6+} to S^{2-} (i.e., $12[FeO] + H_2SO_4 = 4Fe_3O_4$ (Magnetite) + H_2S; [62,68]), so the acid in stage II ore-forming fluids became stronger with an increase in S^{2-} and H^+ activity [69]. More significantly, the homogenization temperatures of stage II fluids were obviously lower than those of the stage I fluids (Figure 6). H–O isotope data in this study indicate that mixing of hydrothermal fluids and meteoric water occurred in stage II. The addition of cooler and lower-salinity meteoric water inevitably led to a decrease in temperature and salinity of the primary hotter and high-salinity magmatic water, causing the precipitation of sulfides. Furthermore, the micro-thermometric data obtained in this study showed that Cu was mainly deposited below 400 °C in stage II, which is consistent with the temperature at which hydrothermal fluids reached Cu saturation in some micro-thermometric and thermodynamic studies of FIs [70–73]. Beyond stage I, fluid boiling also occurred in stage II. Generally, fluid boiling can cause widespread hydraulic fracturing and accelerate the influx and circulation of meteoric water, which could lead to rapid deposition of sulfides. In addition, fluid boiling can lead to the exsolution of volatile components from ore-forming fluids [51], which would also promote the enrichment of metals in the ore-forming fluids [74,75]. Thus, we believe that fluid boiling occurring below 400 °C may be the primary factor for Cu precipitation in the Huoluotai Cu (Mo) deposit.

No evidence of fluid boiling was found in stages III and IV. The ore-forming fluids in stages III and IV belong to a homogeneous H_2O–NaCl system and became more diluted and cool, as indicated by the H−O isotope data. Magmatic water mixed with meteoric water may have initiated metal sulfide precipitation in stage III [71]. The increasing meteoric water influx may have formed the quartz + calcite ± pyrite ± fluorite veins in stage IV, reflecting waning of the hydrothermal system.

7. Conclusions

(1) The Huoluotai Cu (Mo) deposit is a typical porphyry Cu deposit in the NGXR. The ore-forming process of this deposit consists of the sulfide-barren quartz stage (I), the quartz + chalcopyrite ± pyrite ± molybdenite stage (II), the quartz + polymetallic sulfide stage (III), and the quartz + calcite ± pyrite ± fluorite stage (IV). Cu mineralization occurred mainly in stage II.

(2) The results of FI micro-thermometry and H–O isotope analysis showed that the ore-forming fluids originated from a magmatic origin in stage I and then mixed with meteoric water from stages II to IV. The S–Pb isotope results suggest that the source of the ore-forming materials has the characteristics of a crust–mantle-mixing origin.

(3) Fluid boiling occurring below 400 °C may be the primary factor for Cu precipitation in the Huoluotai Cu (Mo) deposit.

Author Contributions: Conceptualization, Y.S., B.L., X.C. and Q.D.; software, F.M., Y.Q. and L.W.; investigation, Y.S., B.L., X.C. and F.M.; data curation, Y.Q. and L.W.; funding acquisition, B.L.; project administration, B.L.; writing—original draft preparation, Y.S.; and writing—review and editing, Y.S. and B.L. All authors have read and agreed to the published version of the manuscript.

Funding: This research was funded by the National Natural Science Foundation of China (41272093), the National Key R&D Program of China (2017YFC0601304), Natural Science Foundation of Jilin Province (No.20180101089JC), Key Projects of Science and Technology Development Plan of Jilin Province (No.20100445), the Shandong Provincial Natural Science Foundation of China (No. ZR2019PD017), Self-determined Foundation of Key Laboratory of Mineral Resources Evaluation in Northeast Asia, Ministry of Natural Resources (DBY-ZZ-19-04), Basic scientific research project of colleges and universities of Liaoning Provincial Department of education in 2021 (LJKZ0369), and the Heilongjiang Research Project of Land and Resources (201605 and 201704).

Data Availability Statement: Not applicable.

Acknowledgments: We would like to thank staffs of the Qiqihaer Institute of Geological Exploration, Heilongjiang, China for sample collection.

Conflicts of Interest: The authors declare no conflict of interest.

References

1. Hu, X.L.; Yao, S.Z.; He, M.C.; Ding, Z.J.; Cui, Y.B.; Shen, J.; Chen, B.; Zhu, B.P. Geochemistry, U–Pb geochronology and Hf isotope studies of the Daheishan porphyry Mo deposit in Heilongjiang Province, NE China. *Resour. Geol.* **2014**, *64*, 102–116. [CrossRef]
2. Liu, J.; Mao, J.W.; Wu, G.; Wang, F.; Luo, D.F.; Hu, Y.Q. Zircon U–Pb and molybdenite Re–Os dating of the Chalukou porphyry Mo deposit in the northern Great Xing'an Range, China and its geological significance. *J. Asian Earth Sci.* **2014**, *79*, 696–709. [CrossRef]
3. Deng, C.Z.; Sun, D.Y.; Han, J.S.; Chen, H.Y.; Li, G.H.; Xiao, B.; Li, R.C.; Feng, Y.Z.; Li, C.L.; Lu, S. Late-stage southwards subduction of the Mongol-Okhotsk oceanic slab and implications for porphyry Cu–Mo mineralization: Constraints from igneous rocks associated with the Fukeshan deposit, NE China. *Lithos* **2019**, *326–327*, 341–357. [CrossRef]
4. Sun, Y.G.; Li, B.L.; Ding, Q.F.; Qu, Y.; Wang, C.K.; Wang, L.L.; Xu, Q.L. Mineralization age and hydrothermal evolution of the Fukeshan Cu (Mo) deposit in the northern Great Xing'an Range, Northeast China: Evidence from fluid inclusions, H–O–S–Pb isotopes, and Re–Os geochronology. *Minerals* **2020**, *10*, 591. [CrossRef]
5. Sun, Y.G.; Li, B.L.; Ding, Q.F.; Meng, F.B.; Chen, X.S.; Qian, Y.; Wang, L.; Wang, L.L.; Xu, Q.L. Timing and ore formation of the Xiaokele porphyry Cu (–Mo) deposit in the northern Great Xing'an Range, NE China: Constraints from geochronology, fluid inclusions, and H–O–S–Pb isotopes. *Ore Geol. Rev.* **2022**, *143*, 104806. [CrossRef]

6. Jahn, B.M.; Wu, F.Y.; Chen, B. Granitoids of the Central Asian Orogenic Belt and continental growth in the Phanerozoic. *Earth Environ. Sci. Trans. R. Soc.* **2000**, *91*, 181–193.
7. Chen, Y.J.; Zhang, C.; Li, N.; Yang, Y.F.; Deng, K. Geology of the Mo deposits in Northeast China. *J. Jilin Univ. (Earth Sci. Ed.)* **2012**, *42*, 1223–1254. (In Chinese)
8. Sun, Y.G. Study on Metallogenesis and Prospecting Direction of Late Jurassic Porphyry Cu (Mo) Deposits in the Northern Segment of the Great Xing'an Range. Ph.D. Thesis, Jilin University, Changchun, China, 2021. (In Chinese with English Abstract).
9. Wang, L. Huoluotai, Mohe Country, Heilongjiang Province Study on Geological Characteristics and Prospecting Direction of Copper Molybdenum Deposit Summary. Master's Thesis, Jilin University, Changchun, China, 2018. (In Chinese with English Abstract).
10. Deng, C.Z.; Li, G.H. The Cu-Mo mineralization of the Late Jurassic porphyry in the Northern Great Xing'an Range: Constraints from zircon U-Pb ages of the Ore-Causative Granites. *Acta Geol. Sin-Engl.* **2019**, *93*, 236–237. [CrossRef]
11. Sun, Y.G.; Li, B.L.; Zhao, Z.H.; Sun, F.Y.; Ding, Q.F.; Chen, X.S.; Li, J.B.; Qian, Y.; Li, Y.J. Age and petrogenesis of late Mesozoic intrusions in the Huoluotai porphyry Cu-(Mo) deposit, northeast China: Implications for regional tectonic evolution. *Geosci. Front.* **2022**, *13*, 101344. [CrossRef]
12. Wu, F.Y.; Sun, D.Y.; Ge, W.C.; Zhang, Y.B.; Grant, M.L.; Wilde, S.A.; Jahn, B.M. Geochronology of the Phanerozoic granitoids in northeastern China. *J. Asian Earth Sci.* **2011**, *41*, 1–30. [CrossRef]
13. Liu, Y.J.; Li, W.M.; Feng, Z.Q.; Wen, Q.B.; Franz, N.; Liang, C.Y. A review of the Paleozoic tectonics in the eastern part of Central Asian Orogenic Belt. *Gondwana Res.* **2017**, *43*, 123–148. [CrossRef]
14. Ge, W.C.; Wu, F.Y.; Zhou, C.Y.; Rahman, A.A. Emplacement age of the Tahe granite and its constraints on the tectonic nature of the Erguna block in the northern part of the Da Hinggan Range. *Chin. Sci. Bull.* **2005**, *50*, 2097–2105. [CrossRef]
15. Zhou, J.B.; Wang, B.; Wilde, S.A.; Zhao, G.C.; Cao, J.L.; Zheng, C.Q.; Zeng, W.S. Geochemistry and U–Pb zircon dating of the Toudaoqiao blueschists in the Great Xing'an Range, northeast China, and tectonic implications. *J. Asian Earth Sci.* **2015**, *97*, 197–210. [CrossRef]
16. IMBGMR (Inner Mongolian Bureau of Geology and Mineral Resources). *Regional Geology of Inner Mongolia*; Geological Publishing House: Beijing, China, 1991; pp. 1–725. (In Chinese)
17. Sun, L.X.; Ren, B.F.; Zhao, F.Q.; Ji, S.P.; Geng, J.Z. Late Paleoproterozoic magmatic records in the Eerguna massif: Evidences from the zircon U–Pb dating of granitic gneisses. *Geol. Bull. China* **2013**, *32*, 341–352, (In Chinese with English Abstract).
18. Ge, W.C.; Chen, J.S.; Yang, H.; Zhao, G.C.; Zhang, Y.L.; Tian, D.X. Tectonic implications of new zircon U–Pb ages for the Xinghuadukou Complex, Erguna Massif, northern Great Xing'an Range, NE China. *J. Asian Earth Sci.* **2015**, *106*, 169–185. [CrossRef]
19. Sun, Y.G.; Li, B.L.; Sun, F.Y.; Ding, Q.F.; Qian, Y.; Li, L.; Xu, Q.L.; Li, Y.J. Geochronology, geochemistry, and Hf isotopic compositions of Early Permian syenogranite and diabase from the northern Great Xing'an Range, NE China: Petrogenesis and tectonic implications. *Can. J. Earth. Sci.* **2020**, *57*, 1478–1491. [CrossRef]
20. IMBGMR (Inner Mongolian Bureau of Geology Mineral Resources). *Lithostratigraphy of Inner Mongolia*; China University of Geosciences Press: Wuhan, China, 1996; pp. 1–342. (In Chinese)
21. Zhang, J.H.; Ge, W.C.; Wu, F.Y.; Wilde, S.A.; Yang, J.H.; Liu, X.M. Large-scale Early Cretaceous volcanic events in the northern Great Xing'an Range, Northeastern China. *Lithos* **2008**, *102*, 138–157. [CrossRef]
22. Tang, J.; Xu, W.L.; Wang, F.; Zhao, S.; Wang, W. Early Mesozoic southward subduction history of the Mongol-Okhotsk oceanic plate: Evidence from geochronology and geochemistry of Early Mesozoic intrusive rocks in the Erguna Massif, NE China. *Gondwana Res.* **2016**, *31*, 218–240. [CrossRef]
23. Gou, J.; Sun, D.Y.; Ren, Y.S.; Hou, X.G.; Yang, D.G. Geochemical and Hf isotopic compositions of Late Triassic–Early Jurassic intrusions of the Erguna Block, Northeast China: Petrogenesis and tectonic implications. *Int. Geol. Rev.* **2017**, *59*, 347–367. [CrossRef]
24. Sun, Y.G.; Li, B.L.; Sun, F.Y.; Ding, Q.F.; Wang, B.Y.; Li, Y.J.; Wang, K. Mineralization events in the Xiaokele porphyry Cu (–Mo) deposit, NE China: Evidence from zircon U–Pb and K–feldspar Ar–Ar geochronology and petrochemistry. *Resour. Geol.* **2020**, *70*, 254–272. [CrossRef]
25. Roedder, E. Fluid Inclusions. *Rev. Mineral. Mich. Mineral. Soc. Am.* **1984**, *12*, 644.
26. Clayton, W.M.; Mayeda, T.K. The use of bromine pent a fluoride in the extraction of oxygen from oxides and silicates for isotopic analysis. *Geochim. Cosmochim. Acta.* **1963**, *27*, 43–52. [CrossRef]
27. Friedman, I. Deuterium content of natural waters and other substances. *Geochim. Cosmochim. Acta* **1953**, *4*, 89–103. [CrossRef]
28. McCrea, J.M. On the isotopic chemistry of carbonates and a paleotemperature scale. *J. Chem. Phys.* **1950**, *18*, 849–857. [CrossRef]
29. Steele-MacInnis, M.; Lecumberri-Sanchez, P.; Bodnar, R.J. HOKIEFLINCS_H_2O-NACL: A Microsoft Excel spreadsheet for interpreting microthermometric data from fluid inclusions based on the PVTX properties of H_2O–NaCl. *Comput. Geosci.* **2012**, *49*, 334–337. [CrossRef]
30. Lecumberri-Sanchez, P.; Steele-MacInnis, M.; Bodnar, R.J. A numerical model to estimate trapping conditions of fluid inclusions that homogenize by halite disappearance. *Geochim. Cosmochim. Acta* **2012**, *92*, 14–22. [CrossRef]
31. Collins, P.L.F. Gas hydrates in CO_2-bearing fluid inclusions and use freezing data for estimation of salinity. *Econ. Geol.* **1979**, *74*, 1435–1444. [CrossRef]

32. Clayton, R.N.; O'Neil, J.R.; Mayeda, T.K. Oxygen isotope exchange between quartz and water. *J. Geophys. Res. Atmos.* **1972**, *77*, 3057–3067. [CrossRef]
33. Taylor, H.P. The application of oxygen and hydrogen isotope studies to problems of hydrothermal alteration and ore deposition. *Econ. Geol.* **1974**, *69*, 843–883. [CrossRef]
34. Friedman, I.; O'Neil, J.R. Complication of Stable Isotope Fractionation Factors of Geochemical Interest. In *Data of Geochemistry*, 6th ed.; Fleischer, M., Ed.; US Government Printing Office: Washington, DC, USA, 1977.
35. Veizer, J.; Hoefs, J. The nature of $^{18}O/^{16}O$ and $^{13}C/^{12}C$ secular trends in sedimentary carbonate rocks. *Geochim. Cosmochim. Acta* **1976**, *40*, 1387–1395. [CrossRef]
36. Hoefs, J. *Stable Isotope Geochemistry*, 6th ed.; Springer: Berlin/Heidelberg, Germany, 2009; pp. 130–135.
37. Taylor, H.P.; Frechen, J.; Degens, E.T. Oxygen and carbon isotope studies of carbonatites from the Laacher See District, West Germany and the Alnö District, Sweden. *Geochim. Cosmochim. Acta* **1967**, *31*, 407–430. [CrossRef]
38. Ohmoto, H. Systematics of sulfur and carbon isotopes in hydrothermal ore deposits. *Econ. Geol.* **1972**, *67*, 551–578. [CrossRef]
39. Ohmoto, H.; Rye, R.O. Isotopes of sulfur and carbon. In *Geochemistry of Hydrothermal Ore Deposits*; Barnes, H.L., Ed.; Wiley: New York, NY, USA, 1979; pp. 509–567.
40. Chaussidon, M.; Albarède, F.; Sheppard, S.M.F. Sulphur isotope variations in the mantle from ion microprobe analyses of micro-sulphide inclusions. *Earth Planet. Sci. Lett.* **1989**, *92*, 144–156. [CrossRef]
41. Field, C.W.; Zhang, L.; Dilles, J.H.; Rye, R.O.; Reed, M.H. Sulfur and oxygen isotopic record in sulfate and sulfide minerals of early, deep, pre-main stage porphyry Cu–Mo and late main stage base-metal mineral deposits, Butte district, Montana. *Chem. Geol.* **2005**, *215*, 61–93. [CrossRef]
42. Salas, R.D.; Ochoa-Landin, L.; Ruiz, J.; Eastoe, C.; Meza-Figueroa, D.; Zuniga-Hernandez, H.; Mendivil-Quijada, H.; Quintanar-Ruiz, F. Geology, stable isotope, and U-Pb geochronology of the Mariquita porphyry copper and Lucy Cu-Mo deposits, Cananea District, Mexico: A contribution to regional exploration. *J. Geochem. Explor.* **2013**, *124*, 140–154. [CrossRef]
43. Liu, J.; Mao, J.W.; Wu, G.; Wang, F.; Luo, D.F.; Hu, Y.Q. Fluid inclusions and H–O–S–Pb isotope systematics of the Chalukou giant porphyry Mo deposit, Heilongjiang Province, China. *Ore Geol. Rev.* **2014**, *59*, 83–96. [CrossRef]
44. Zhang, F.F.; Wang, Y.H.; Liu, J.J.; Wang, J.P.; Zhao, C.B.; Song, Z.W. Origin of the Wunugetushan porphyry Cu–Mo deposit, Inner Mongolia, NE China: Constraints from geology, geochronology, geochemistry, and isotopic compositions. *J. Asian Earth Sci.* **2016**, *117*, 208–224. [CrossRef]
45. Mi, K.F.; Liu, Z.J.; Li, C.F.; Liu, R.B.; Wang, J.P.; Peng, R.M. Origin of the Badaguan porphyry Cu-Mo deposit, Inner Mongolia, northeast China: Constraints from geology, isotope geochemistry and geochronology. *Ore Geol. Rev.* **2017**, *81*, 154–172. [CrossRef]
46. Huang, M.L.; Bi, X.W.; Gao, J.F.; Xu, L.L.; Xiao, J.F.; Liu, S.T.; Wang, X.S.; Zhou, T. Sulfur and lead isotopic variations in the giant Yulong porphyry Cu (Mo-Au) deposit from the eastern Tibetan Plateau: Implications for origins of S and Pb, and metal precipitation. *J. Geochem. Explor.* **2019**, *197*, 70–83. [CrossRef]
47. Zartman, R.; Doe, B. Plumbotectonics: The model. *Tectonophysics* **1981**, *75*, 135–162. [CrossRef]
48. Roedder, E.; Bodnar, R.J. Geologic pressure determinations from fluid inclusion studies. *Annu. Rev. Earth Planet. Sci.* **1980**, *8*, 263–301. [CrossRef]
49. Brown, P.E.; Hagemann, S.G. Macflincor and its application to fluids in Archean lode-gold deposits. *Geochim. Cosmochim. Acta* **1995**, *59*, 3943–3952. [CrossRef]
50. Driesner, T.; Heinrich, C.A. The system H_2O–NaCl. Part I: Correlation formulae for phase relations in temperature–pressure-composition space from 0 to 1000 °C, 0 to 5000 bar, and 0 to 1 XNaCl. *Geochim. Cosmochim. Acta* **2007**, *71*, 4880–4901.
51. Bowers, T.S.; Helgeson, H.C. Calculation of the thermodynamic and geochemical consequences of nonideal mixing in the system H_2O-CO_2-NaCl on phase relations in geologic systems: Equation of state for H_2O-CO_2-NaCl fluids at high pressures and temperatures. *Geochim. Cosmochim. Acta* **1983**, *47*, 1247–1275. [CrossRef]
52. Joyce, D.B.; Holloway, J.R. An experimental determination of the thermodynamic properties of H_2O-CO_2-NaCl fluids at high pressures and temperatures. *Geochim. Cosmochim. Acta* **1993**, *57*, 733–746. [CrossRef]
53. Gehrig, M.; Lentz, H.; Franck, E. The system water-carbon dioxide-sodium chloride to 773 K and 300 MPa. *Phys. Chem.* **1986**, *90*, 525–533. [CrossRef]
54. Rusk, B.G.; Reed, M.; Dilles, J.H. Fluid inclusion evidence for magmatic-hydrothermal fluid evolution in the porphyry copper-molybdenum deposit at Butte, Montana. *Econ. Geol.* **2008**, *103*, 307–332. [CrossRef]
55. Hedenquist, J.W.; Lowenstern, J.B. The role of magmas in the formation of hydrothermal ore deposits. *Nature* **1994**, *370*, 519–527. [CrossRef]
56. Barnes, H.L. Solubilities of ore minerals. In *Geochemistry of Hydrothermal Ore Deposits*; Barnes, H.L., Ed.; Wiley: New York, NY, USA, 1979; pp. 404–460.
57. Rye, R.O. The evolution of magmatic fluids in the epithermal environment: The stable isotope perspective. *Econ. Geol.* **1993**, *88*, 733–752. [CrossRef]
58. Harris, A.C.; Golding, S.D. New evidence of magmatic-fluid-related phyllic alteration: Implications for the genesis of porphyry Cu deposits. *Geology* **2002**, *30*, 335–338. [CrossRef]
59. Chen, Y.J.; Zhang, C.; Wang, P.; Pirajno, F.; Li, N. The Mo deposits of Northeast China: A powerful indicator of tectonic settings and associated evolutionary trends. *Ore Geol. Rev.* **2017**, *81*, 602–640.

60. Seedorff, E.; Dilles, J.H.; Proffett, J.M.; Einaudi, M.T.; Zurcher, L.; Stavast, W.J.A.; Johnson, D.A.; Barton, M.D. Porphyry deposits: Characteristics and origin of hypogene features. *Econ. Geol.* **2005**, *100*, 251–298.
61. Sun, W.D.; Huang, R.F.; Li, H.; Hu, Y.B.; Zhang, C.C.; Sun, S.J.; Zhang, L.P.; Ding, X.; Li, C.Y.; Zartman, R.E.; et al. Porphyry deposits and oxidized magmas. *Ore Geol. Rev.* **2015**, *65*, 97–131. [CrossRef]
62. Mungall, J.E. Roasting the mantle: Slab melting and the genesis of major Au and Au-rich Cu deposits. *Geology* **2002**, *30*, 915–918. [CrossRef]
63. Chen, Y.J.; Pirajno, F.; Li, N.; Guo, D.S.; Lai, Y. Isotope systematic and fluid inclusion studies of the Qiyugou breccias pipe-hosted gold deposit, Qinling Orogen, Henan Province, China: Implications for ore genesis. *Ore Geol. Rev.* **2009**, *35*, 245–261.
64. Li, N.; Ulrich, T.; Chen, Y.-J.; Thomsen, T.B.; Pease, V.; Pirajno, F. Fluid evolution of the Yuchiling porphyry Mo deposit, East Qinling, China. *Ore Geol. Rev.* **2012**, *48*, 442–459. [CrossRef]
65. Yang, Y.F.; Li, N.; Chen, Y.J. Fluid inclusion study of the Nannihu giant porphyry Mo–W deposit, Henan Province, China: Implications for the nature of porphyry ore-fluid systems formed in a continental collision setting. *Ore Geol. Rev.* **2012**, *46*, 83–94. [CrossRef]
66. Ulrich, T.; Guenther, D.; Heinrich, C.A. Gold concentrations of magmatic brines and the metal budget of porphyry copper deposits. *Nature* **1999**, *399*, 676–679. [CrossRef]
67. Heinrich, C.A. The physical and chemical evolution of low-salinity magmatic fluids at the porphyry to epithermal transition: A thermodynamic study. *Miner. Depos.* **2005**, *39*, 864–889.
68. Liang, H.Y.; Sun, W.D.; Su, W.C.; Zartman, R.E. Porphyry copper-gold mineralization at Yulong, China, promoted by decreasing redox potential during magnetite alteration. *Econ. Geol.* **2009**, *104*, 587–596. [CrossRef]
69. Sillitoe, R.H. Porphyry copper systems. *Econ. Geol.* **2010**, *105*, 3–41. [CrossRef]
70. Fournier, R.O. Hydrothermal process related to movement of fluid from plastic into brittle rock in the magmatic-epithermal environment. *Econ. Geol.* **1999**, *94*, 1193–1211. [CrossRef]
71. Hezarkhani, A.; William-Jones, A.E.; Gammons, C.H. Factors controlling copper solubility and chalcopyrite deposition in the Sungun porphyry copper deposit, Iran. *Miner. Dep.* **1999**, *34*, 770–783. [CrossRef]
72. Williams, P.J.; Dong, G.Y.; Ryan, C.G.; Pollard, P.J.; Rotherham, J.F.; Mernagh, T.P.; Chapman, L.H. Geochemistry of hypersaline fluid inclusions from the Starra (Fe oxide)-Au-Cu deposit, Cloncurry district, Queensland. *Econ. Geol. Bull. Soc. Econ. Geol.* **2001**, *96*, 875–883.
73. Landtwing, M.R.; Pettke, T.; Halter, W.E.; Heinrich, C.A.; Redmond, P.B.; Einaudi, M.T.; Kunze, K. Copper deposition during quartz dissolution by cooling magmatic–hydrothermal fluids: The Bingham porphyry. *Earth Planet. Sci. Lett.* **2005**, *235*, 229–243. [CrossRef]
74. Harris, A.C.; Kamenetsky, V.S.; White, N.C.; Achterbergh, E.V.; Ryan, C.G. Melt inclusions in veins: Linking magmas and porphyry Cu deposits. *Science* **2003**, *302*, 2109–2111. [CrossRef] [PubMed]
75. Zhu, J.J.; Hu, R.Z.; Richards, J.P.; Bi, X.W.; Zhong, H. Genesis and Magmatic Hydrothermal Evolution of the Yangla Skarn Cu Deposit, Southwest China. *Econ. Geol.* **2015**, *110*, 631–652. [CrossRef]